

# Simulations of Three-dimensional Nematic Guidance of Microswimmers

Zeyang Mou,<sup>1</sup> Yuan Li,<sup>2</sup> Zhihong You,<sup>2</sup> and Rui Zhang<sup>1,\*</sup>

<sup>1</sup>*Department of Physics, Hong Kong University of Science and Technology, Clear Water Bay, Kowloon, Hong Kong SAR*

<sup>2</sup>*Fujian Provincial Key Laboratory for Soft Functional Materials Research,  
Research Institute for Biomimetics and Soft Matter,*

*Department of Physics, Xiamen University, Xiamen, Fujian 361005, China*

(Dated: January 15, 2025)

It has been shown that an anisotropic liquid crystalline (LC) environment can be used to guide the self-propulsion dynamics of dispersed microswimmers, such as bacteria. This type of composite system is named “living nematic” (LN). In the dilute limit, bacteria are found to mainly follow the local director field. Beyond the dilute limit, however, they exhibit novel dynamical behaviors, from swirling around a spiral +1 defect pattern to forming undulating waves, and to active turbulence. Our current knowledge of how these different behaviors emerge at different population densities remains limited. Here we develop a hybrid method to simulate the dynamics of microswimmers dispersed in a nematic LC. Specifically, we model the microswimmers using active Brownian dynamics method, which is coupled to a hydrodynamic model of nematic LCs to describe the evolution of the flow field and the LC structure. Our method is validated by comparing to existing quasi-two-dimensional (2D) experiments, including undulated swirling around a spiral pattern and stabilized undulated jets on a periodic C-pattern. We further extend our method to three-dimensional (3D) systems by examining loop-defect dynamics. We find that the morphodynamics and destiny of a loop defect not only depend on the activity (self-propulsion velocity), effective size, and the initial distribution of the swimmers, but also rely on its winding profile. Specifically, +1/2 wedge and radial twist winding can dictate the dynamics of loop defects. By varying the characteristic reversal time, we predict that microswimmers not necessarily accumulate in splay regions. Taken together, our hybrid method provides a faithful tool to explain and guide the experiments of LNs in both 2D and 3D, sheds light on the interplay between microswimmer distribution and defect dynamics, and unravels the design principles of using LCs to control active matter.

## I. INTRODUCTION

Suspensions of microswimmers are a prototypical active matter, in which individual swimmers can self-propel by converting other forms of energy into mechanical work [1–3]. The individual and collective behaviors of microswimmers exhibit significant variability depending on several factors, including their species (which can be synthetic, such as robots or self-phoretic colloids, or living organisms, like bacteria and cytoskeletal extracts), population density, and the properties of the dispersing medium [4, 5]. Existing work has extensively investigated Newtonian suspensions of microswimmers. The scope of the continuous phase extends beyond isotropic solution such as water. In many biological and physiological contexts, microswimmers navigate through a complex, anisotropic medium. Notable examples include sperm cells in cervical mucus [6, 7], bacteria or cells swimming in extracellular DNA biofilm matrix [8–11], synthetic microswimmers for drug delivery [12–14], and *Trypanosoma brucei* [15] moving through blood and lymphatic. The anisotropic and viscoelastic properties of the environment play a crucial role in modulating the dynamics of the dispersed swimmers, thereby offering a potential approach to control their dynamical behaviors [16–21].

A typical anisotropic medium is liquid crystal (LC).

In the recent decade, non-toxic lyotropic chromonic LCs have been utilized to control the swimming behavior of dispersed bacteria [22], including *E. coli* [23], *B. subtilis* [22, 24–29], and *P. mirabilis* [30–32]. This type of composite system is named “living nematic” (LN) [24]. In the dilute limit, these bacteria tend to swim along the local nematic director due to a strong anisotropic viscous coefficient [24]. However, theoretical analyses and simulations indicate that the microswimmer’s type, whether being a “pusher” or a “puller” [33, 34], and its surface anchoring type and strength [33, 35], can modify its preferred swimming direction. When the microswimmers are dense enough, they can interact with each other in an anisotropic manner [25, 30]. But more importantly, they can generate an active stress, which can induce elastic distortions to the background nematic, giving rise to the so-called “active turbulent” state, which is characterized by persistent proliferation, motion, and annihilation of topological defects [22, 24, 27, 28]. In a quasi two-dimensional (2D) film, extensile microswimmers can induce bend instability in an otherwise uniform nematic [22, 24, 26–29]. Whereas in a three-dimensional (3D) cell, they can trigger a twist-bend instability as a result of the competition between different elastic modes and the active stress [34].

To control spontaneous flows and microswimmer dynamics in LNs, surface patterning technique has been proven promising [22, 26–28], which can also suppress or stabilize instability patterns [27, 29]. Surface alignment (anchoring) condition can dictate the 3D trajectories of

---

\* ruizhang@ust.hk (R.Z)

the microswimmers through controlling the bulk nematic field [31, 36]. If the substrates of a nematic cell impose a planar anchoring condition, bacteria tend to swim within the midplane of the cell. Whereas if the substrates favor homeotropic anchoring, bacteria tend to swim in the bulk or form coordinated, trainlike groups [31, 36]. Hybrid cells with planar and homeotropic surfaces further create nontrivial 3D trajectories, confining bacteria near the planar plate where splay deformation dominates [31].

To elucidate bacterial dynamics in LNs, various types of continuum models have been developed. Spherical or ellipsoidal squirmer model has been used to represent individual microswimmers in an LN [33–35]. When the bacterial size and shape are not essential, point-particle approximation can be adopted to study their collective dynamics [26, 37]. At a more coarse-grained level, an advection-diffusion equation for the bacterial concentration field can be used to describe the temporal behavior of bacterial distribution in an LN [27, 28]. Alternatively, bacteria-rich regions can be modeled as an active nematic phase in a biphasic LC model [29]. These models provide useful insights into individual microswimmer behavior in an LC and their concentration modulation by topological defects.

Despite a relatively good understanding of LNs in dilute and dense limits, as revealed by the aforementioned models, and the promising applications of patterned surfaces to guide bacterial dynamics, it remains unclear what happens under certain conditions, e.g., in the semidilute condition, instability patterns can stop growing and become stabilized. Additionally, a related question remains unanswered: how do dilute-limit bacterial dynamics transition into dense-limit collective behavior as bacterial concentration gradually increases?

To address these open questions, here we develop a hybrid simulation method, which can quantitatively describe nematodynamics while accounting for arbitrary number of microswimmers. Specifically, we combine an agent-based method [26, 37] and a hydrodynamic model [38] to simulate self-propelled point-like particles in 2D and/or 3D nematic LCs. A similar hybrid approach has been successful in modeling aqueous solutions of microswimmers [39, 40]. We validate our computational model by reproducing key phenomena in previous experimental and numerical results [22, 26, 27, 29]. We further use the model to examine the dynamics of microswimmers in a 3D nematic cell with and without topological defects. We also take into account the reversal of bacterial swimming direction in our simulation and find that depending on the reversal time scale, they are not necessarily accumulating in planar-anchoring walls. Taken together, we have developed a 3D simulation method to model LNs, facilitating further research in using anisotropic media to guide microswimmers.

## II. MODEL

### A. Agent-based Model to Simulate Microswimmers

We model active particles (e.g., microswimmers in the experiment) as point particles with a constant self-propelled velocity  $v_0$  along a direction represented by a unit vector  $\hat{\mathbf{p}}_i$  for the  $i$ 'th swimmer. In this work, we occasionally use swimmer and particle interchangeably to refer to microswimmer. Its equation of motion is governed by an over-damped active Brownian dynamics equation

$$\partial_t \mathbf{r}_i = v_0 \hat{\mathbf{p}}_i + \gamma_{LJ} \mathbf{F}_i + \mathbf{u}, \quad (1)$$

where  $\mathbf{u}$  is the velocity vector representing the background flow, and  $\mathbf{F}_i = -\nabla_{\mathbf{r}_i} \sum_{i < j} V(\mathbf{r}_{ij})$  is the Lennard–Jones-like force to describe the excluded volume interactions between particle  $i$  and  $j$ , which is derived from the following potential function

$$V(\mathbf{r}_{ij}) = \begin{cases} 4\varepsilon_{LJ} \left[ \left( \frac{\sigma}{r_{ij}} \right)^{12} - \left( \frac{\sigma}{r_{ij}} \right)^6 \right], & r_{ij} \leq 2^{1/6} \sigma, \\ 0, & r_{ij} > 2^{1/6} \sigma \end{cases}, \quad (2)$$

where  $r_{ij} = |\mathbf{r}_{ij}|$  is the distance between the two microswimmers,  $\varepsilon_{LJ}$  is the interaction energy scale, and  $\sigma$  is the characteristic (excluded-volume) size of the microswimmer.

Microswimmers tend to align with the local director field denoted by a unit vector  $\hat{\mathbf{n}}$ . A torque is acted on the orientation vector  $\hat{\mathbf{p}}_i$  about an axis  $\mathbf{w}_s$ , which can be expressed as  $\mathbf{w}_s = 2\gamma_B (\hat{\mathbf{p}}_i \cdot \hat{\mathbf{n}}) (\hat{\mathbf{p}}_i \times \hat{\mathbf{n}}) = |\mathbf{w}_s| \hat{\mathbf{s}}$ , where  $\gamma_B$  is a coupling parameter,  $\hat{\mathbf{s}}$  is a unit vector denoting the rotation axis, and the magnitude  $|\mathbf{w}_s|$  is the angular velocity of the orientation vector  $\hat{\mathbf{p}}_i$ , namely  $\Delta\theta = |\mathbf{w}_s| \Delta t$  for an infinitesimal duration of time  $\Delta t$ . To update  $\hat{\mathbf{p}}_i$  in the simulation, we introduce the rotation matrix  $\mathcal{R}$ , which is implemented using the Rodrigues formalism [41]:

$$\mathcal{R}(\Delta\theta) = e^{\Delta\theta \mathbf{s}_\times} = \mathbf{I} + \sin \Delta\theta \mathbf{s}_\times + (1 - \cos \Delta\theta) \mathbf{s}_\times^2, \quad (3)$$

where the skew-symmetric matrix  $[\mathbf{s}_\times]$  is defined as:

$$[\mathbf{s}_\times] = \begin{bmatrix} 0 & -s_z & s_y \\ s_z & 0 & -s_x \\ -s_y & s_x & 0 \end{bmatrix}. \quad (4)$$

The updated orientation vector at time  $t + \Delta t$  is then given by  $\hat{\mathbf{p}}_i(t + \Delta t) = \mathcal{R}(\Delta\theta) \hat{\mathbf{p}}_i(t)$ , and the time derivative of  $\hat{\mathbf{p}}_i$  aligns with the angular velocity as  $\partial_t \hat{\mathbf{p}}_i = \mathbf{w}_s \times \hat{\mathbf{p}}_i$ .

Additionally, we consider the reorientation of the microswimmer in the presence of a background flow field. This reorientation is described by  $\partial_t \hat{\mathbf{p}}_i = \frac{1}{2} \boldsymbol{\omega} \times \hat{\mathbf{p}}_i + B (\mathbf{E} \cdot \hat{\mathbf{p}}_i - (\hat{\mathbf{p}}_i \cdot \mathbf{E} \cdot \hat{\mathbf{p}}_i) \hat{\mathbf{p}}_i)$ , which originates from Jeffrey's equation [37, 42]. Here,  $\boldsymbol{\omega} = \nabla \times \mathbf{u}$  represents the vorticity, and  $\mathbf{E} = \frac{1}{2} (\nabla \mathbf{u} + (\nabla \mathbf{u})^T)$  is the strain-rate tensor. The parameter  $B$ , known as the Bretherton parameter, is defined as  $B = (e^2 - 1)/(e^2 + 1)$ , where  $e = 2.2$

is the aspect ratio of the microswimmer used in our simulations [26].

Finally, the evolution of the orientation vector  $\hat{\mathbf{p}}_i$  for particle  $i$  is expressed as:

$$\begin{aligned} \partial_t \hat{\mathbf{p}}_i = & (\mathbf{w}_s + \frac{1}{2}\boldsymbol{\omega}) \times \hat{\mathbf{p}}_i + B(\mathbf{E} \cdot \hat{\mathbf{p}}_i - (\hat{\mathbf{p}}_i \cdot \mathbf{E} \cdot \hat{\mathbf{p}}_i)\hat{\mathbf{p}}_i) \\ & + D_r \xi(t) \hat{\mathbf{p}}_i^\perp, \end{aligned} \quad (5)$$

where the third term introduces a white noise  $\xi(t)$  with time de-correlated and normalized amplitude  $\langle \xi(t)\xi(t') \rangle = \delta(t, t')$ , and  $\hat{\mathbf{p}}_i^\perp$  represents a unit vector perpendicular to  $\hat{\mathbf{p}}_i$ .

In 2D simulations, the orientation vector for particle  $i$  can be represented by its orientation angle  $\theta_i^p$  via  $\hat{\mathbf{p}}_i = (\cos \theta_i^p, \sin \theta_i^p)$ . Likewise, the nematic director can also be rewritten in terms of the director angle  $\theta$  through  $\hat{\mathbf{n}} = (\cos \theta, \sin \theta)$ . Thus, the orientational equation of motion Eq. 5 can be simplified as

$$\begin{aligned} \partial_t \theta_i^p = & \gamma_B \sin[2(\theta - \theta_i^p)] + \frac{1}{2}\omega_z \\ & + \frac{1}{2}B[(E_{yy} - E_{xx})\sin(2\theta_i^p) + 2E_{xy}\cos(2\theta_i^p)] \\ & + D_r \xi(t). \end{aligned} \quad (6)$$

### B. Continuum Model to Solve the Nematic Directors and the Velocity Field

We employ a hybrid lattice Boltzmann method (LBM) to perform simulations to solve the nematic director field and the flow field [43]. The microstructure of the nematic liquid crystal is characterized by a traceless, symmetric tensorial order parameter  $\mathbf{Q}$ . For a uniaxial nematic LC,  $\mathbf{Q} = S(\mathbf{nn} - \mathbf{I}/3)$ , where  $S$  is the scalar order parameter. The governing equation of the  $\mathbf{Q}$ -tensor is described by the Beris-Edwards equation [38, 44]:

$$\partial_t \mathbf{Q} + \mathbf{u} \cdot \nabla \mathbf{Q} - \mathbf{S} = \Gamma \mathbf{H}. \quad (7)$$

By defining the symmetric part and the antisymmetric part of the velocity gradient tensor  $\mathbf{E} = \frac{1}{2}(\nabla \mathbf{u} + (\nabla \mathbf{u})^T)$  and the vorticity tensor  $\mathbf{W} = \frac{1}{2}(\nabla \mathbf{u} - (\nabla \mathbf{u})^T)$ , the corotation term that determines the alignment of the elongated units in response to the velocity gradient is given by  $\mathbf{S} = (\xi \mathbf{E} + \mathbf{W}) \cdot (\mathbf{Q} + \frac{\mathbf{I}}{3}) + (\mathbf{Q} + \frac{\mathbf{I}}{3}) \cdot (\xi \mathbf{E} - \mathbf{W}) - 2\xi(\mathbf{Q} + \frac{\mathbf{I}}{3})(\mathbf{Q} : \nabla \mathbf{u})$ . We choose the flow-aligning parameter  $\xi = 0.3$  in this study to simulate the flow-tumbling nematic [45].  $\Gamma$  controls the relaxation rate of the director;  $\mathbf{H}$  denotes the molecular field which drives the system towards the thermodynamic equilibrium,  $\mathbf{H} = -\left(\frac{\delta F}{\delta \mathbf{Q}} - \frac{1}{3}\text{Tr}\left(\frac{\delta F}{\delta \mathbf{Q}}\right)\right)$ , where the total free energy  $F = \int_V (f_{\text{LdG}} + f_{\text{ela}}) dV + \int_{\partial V} f_s dS$  contains the

Landau-de Gennes free energy density

$$\begin{aligned} f_{\text{LdG}} = & \frac{A_0}{2} \left(1 - \frac{U}{3}\right) \text{Tr}(\mathbf{Q}^2) - \frac{A_0 U}{3} \text{Tr}(\mathbf{Q}^3) \\ & + \frac{A_0 U}{4} (\text{Tr}(\mathbf{Q}^2))^2, \end{aligned} \quad (8)$$

the elastic energy density

$$f_{\text{ela}} = \frac{1}{2} L Q_{ij,k} Q_{ij,k}, \quad (9)$$

and the surface anchoring energy  $f_s = \frac{1}{2} W (\mathbf{Q} - \mathbf{Q}^s)^2$ , with  $\mathbf{Q}^s$  denoting the preferred order parameter by the surface. In the simulation, the nematic coherence length is fixed to  $\xi_N = \sqrt{\frac{L}{A_0}} = 1$ .

The flow field obeys the incompressibility equation

$$\nabla \cdot \mathbf{u} = 0, \quad (10)$$

and the Navier-Stokes equation

$$\rho_f (\partial_t \mathbf{u} + \mathbf{u} \cdot \nabla \mathbf{u}) = \nabla \cdot (\mathbf{\Pi}^p + \mathbf{\Pi}^a). \quad (11)$$

The passive stress tensor is defined as  $\mathbf{\Pi}_{\alpha\beta}^p = 2\eta E_{\alpha\beta} - P_0 \delta_{\alpha\beta} - \xi H_{\alpha\gamma} (Q_{\gamma\beta} + \frac{1}{3}\delta_{\gamma\beta}) - \xi (Q_{\alpha\gamma} + \frac{1}{3}\delta_{\alpha\gamma}) H_{\gamma\beta} + 2\xi (Q_{\alpha\beta} + \frac{1}{3}\delta_{\alpha\beta}) Q_{\gamma\epsilon} H_{\gamma\epsilon} - \partial_\beta Q_{\gamma\epsilon} \frac{\delta F}{\delta \partial_\alpha Q_{\alpha\epsilon}} + Q_{\alpha\gamma} H_{\gamma\beta} - H_{\alpha\gamma} Q_{\gamma\beta} - \zeta Q_{\alpha\beta}$ , where  $\eta$  is the isotropic viscosity,  $\rho_f$  is the fluid density, and  $P_0$  denotes the hydrostatic pressure. The active stress tensor stems from the microswimmers,  $\mathbf{\Pi}^a = -\alpha \sum_i f(\mathbf{r} - \mathbf{r}_i) \mathbf{Q}_i^B$ , where  $\mathbf{Q}_i^B = (\hat{\mathbf{p}}_i \hat{\mathbf{p}}_i - \mathbf{I}/3)$  denotes the orientation of the microswimmers.  $\alpha_B(\mathbf{r}) = \alpha \sum_i f(\mathbf{r} - \mathbf{r}_i)$  represents the spatially varying activity determined by the distributions of the microswimmers. Here, the kernel  $f(\mathbf{r} - \mathbf{r}_i)$  describes the spatial influence of a microswimmer at position  $\mathbf{r}_i$  on the activity at position  $\mathbf{r}$ . These microswimmers are characterized as pushers ( $\alpha > 0$ ) [46], generating hydrodynamic force dipoles typical of many flagellated bacteria in isotropic solutions [47–52]. The axisymmetric shape of the microswimmer is described by an anisotropic-Gaussian-like distribution [26]

$$\begin{aligned} f(\mathbf{r} - \mathbf{r}_i) = & \frac{1}{(2\pi)^{d/2} g_{\parallel} g_{\perp}^{d-1}} \exp \left[ -\frac{((\mathbf{r} - \mathbf{r}_i) \cdot \hat{\mathbf{p}}_i)^2}{g_{\parallel}^2} \right. \\ & \left. - \frac{|\mathbf{r} - \mathbf{r}_i - ((\mathbf{r} - \mathbf{r}_i) \cdot \hat{\mathbf{p}}_i) \hat{\mathbf{p}}_i|^2}{g_{\perp}^2} \right], \end{aligned} \quad (12)$$

where  $g_{\parallel}$  and  $g_{\perp}$  ( $g_{\parallel}/g_{\perp} = e$ ,  $g_{\perp} = l$ ) define the width of the distribution along the rotational symmetry axis and the direction perpendicular to it, respectively.

In the following simulations, parameters used are:  $\gamma_B = 0.004$ ,  $\varepsilon_{LJ} = 4.167 \times 10^{-4}$ ,  $\gamma_{LJ} = 0.1$ ,  $D_r = 1 \times 10^{-5}$ ,  $\Gamma = 0.1$ ,  $A_0 = 0.01$ ,  $U = 0.35$ ,  $L = 0.01$ ,  $W = 1$ ,  $\rho_f = 1$ , and  $\eta = 0.33$ .



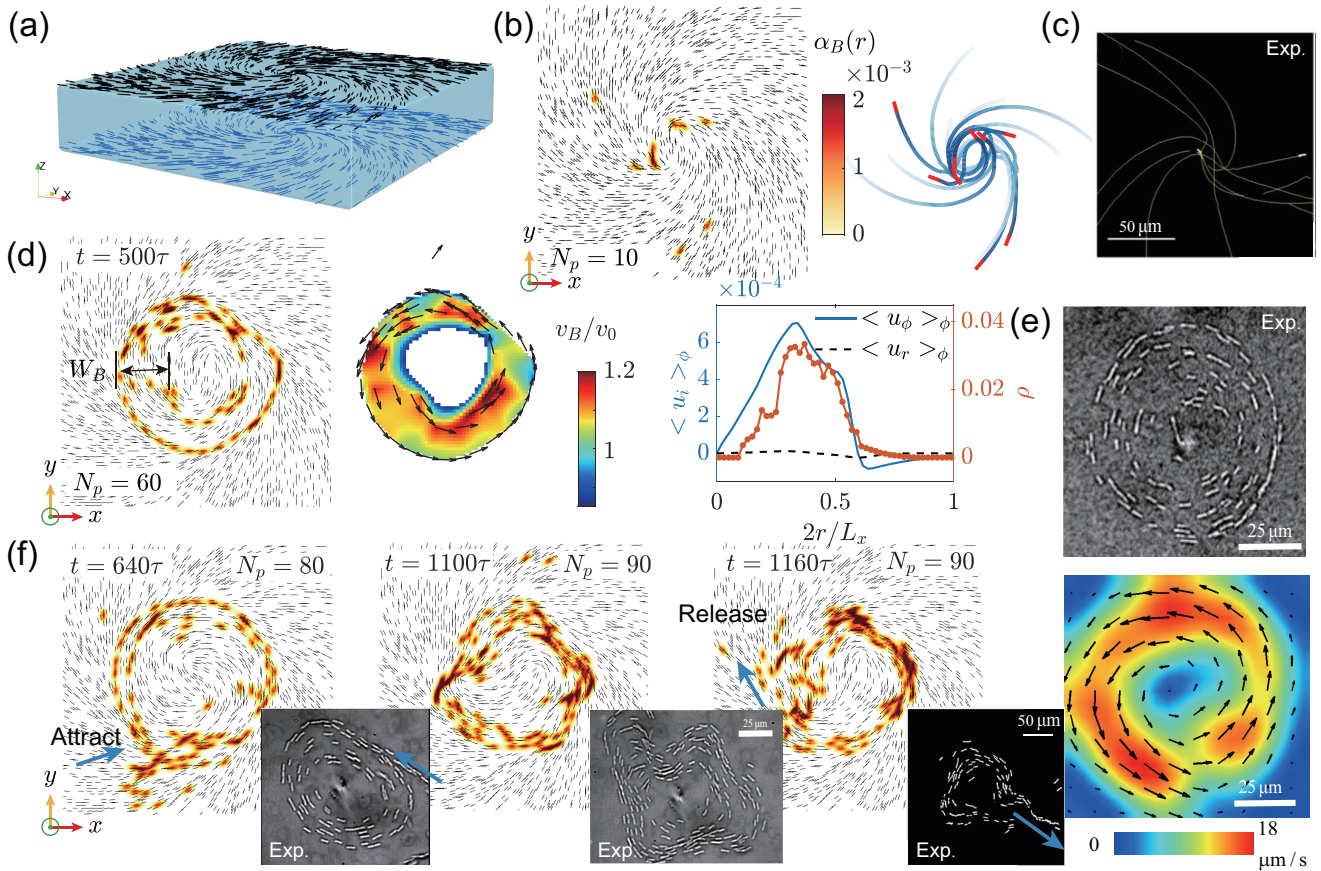


FIG. 1. Microswimmer dynamics on a spiral +1 defect pattern. (a) The schematic of the simulation box with a spiral pattern on both top and bottom surfaces. The dimensions of the box are defined by  $L_x$ ,  $L_y$  and  $L_z$ . (b) Configuration with small amount of bacteria  $N_p = 10$ . Black sticks represent the nematic director, while color indicates the function  $\alpha_B(\mathbf{r})$ , signifying the positions of individual microswimmers. The right panel illustrates swimmer trajectories with red rods marking their final positions. (c) Experimental optical microscopy showing bacteria trajectories that follow the surface-imposed nematic directors at low concentration [26]. (d) Numerical results of stable swirling at higher population  $N_p = 60$ . The left and middle panel show the position and the particle velocity  $v_B$  at  $t = 500\tau$ . The right panel is the azimuthal average of the average flow field from  $t = 450\tau$  to  $t = 600\tau$  ( $\tau = 100$  time steps in simulation) in tangential ( $u_\phi$ ) and radial direction ( $u_r$ ) as a function of the distance to the origin. There are 40 swimmers initially, we add 20, 20, 10 particles at  $t = 300\tau$ ,  $600\tau$  and  $900\tau$ , respectively. (e) Experimental observations of the stable swirling [22]. The color map depicts bacterial velocity. (f) Numerical results initiated from  $t = 0$  of (d). The attraction of outer bacteria to the swirl at  $t = 640\tau$ , undulation at  $t = 1100\tau$ , and release from protrusions at  $t = 1160\tau$ . The experimental snapshots are from Refs. [22, 26].

### III. RESULTS AND DISCUSSION

#### A. Unidirectional swimming using Patterned Surfaces

We first study the dynamics of microswimmers over a spiral-patterned surface in a thin nematic cell [22, 26]. The simulation setup is shown in Fig. 1(a), where we apply the same clockwise-spiral +1 defect pattern on both surfaces with strong anchoring ( $W = 1$ ). For simplicity, the dynamics of the microswimmers are governed by the 2D equations 1 and 6. When the microswimmer population number  $N_p$  is low (up to  $N_p = 10$ ), they are found to roughly align with the designated nematic field, and can move away from the spiral center after entering it (Fig. 1(b)). This behavior is consistent with the experiment of a dilute LN [26] (Fig. 1(c)). As the population

increases to  $N_p = 60$ , the microswimmers do not faithfully follow the clockwise spiral pattern; instead, they are persistently swirling counterclockwise, generating a stable vortex flow (Fig. 1(d)). The central +1 defect splits into two +1/2 defects that orbit the center counterclockwise due to the active flow. The colormap of the swimmer velocity matches well with the experiment [22] (Fig. 1(e)). We further measure the azimuthally averaged flow velocity in the polar coordinate,  $\langle u_r \rangle_\phi$  and  $\langle u_\phi \rangle_\phi$  (Fig. 1(e)). The azimuthal velocity peak matches with the density distribution of the swimmers, which also exhibits a finite width (Figs. 1(d) and 1(e)). This contrasts with a previous particle-based model in which the swimmers are localized to a circular ring [26].

As demonstrated in Fig. 1(f) and Supplementary Video 1, once a stable swirl of  $N_p = 80$  microswimmers is established at  $t = 640\tau$ , 10 more swimmers are added to



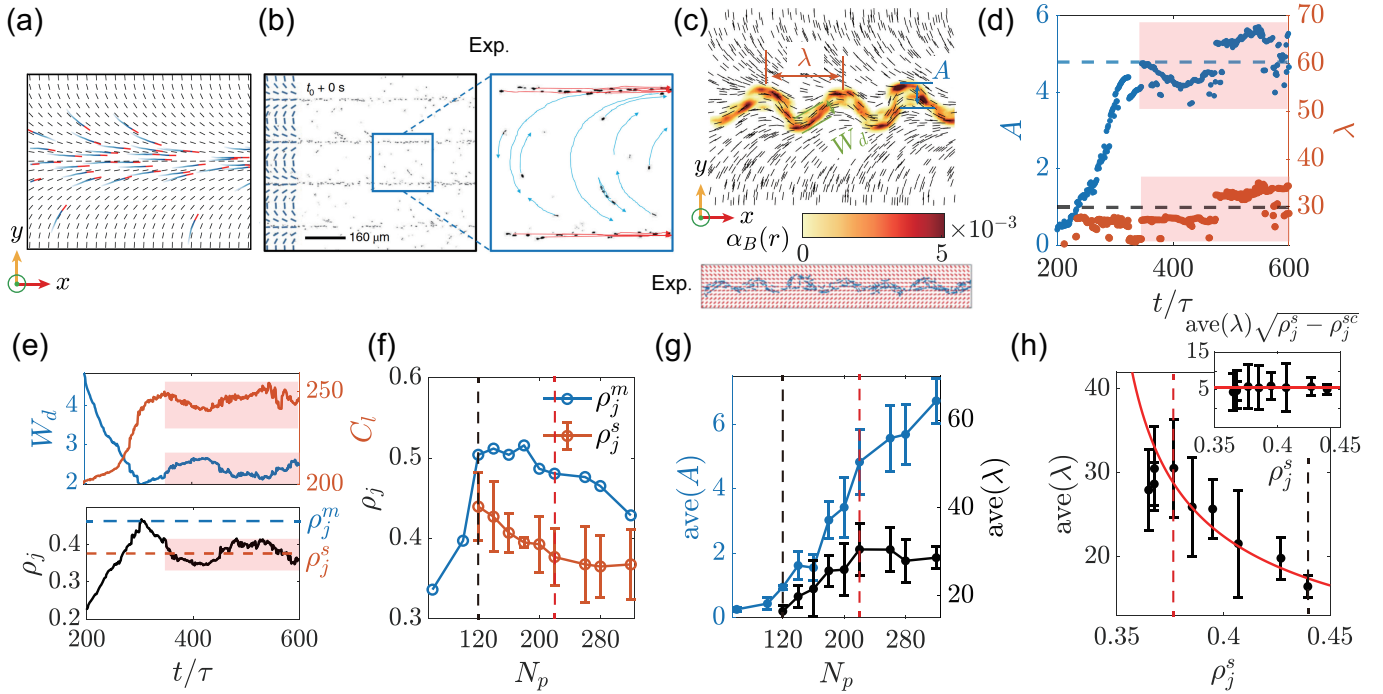


FIG. 2. Polar jets and their undulation over a periodic splay-bend “C”-pattern. (a) Simulated microswimmer trajectories at low concentration with  $N_p = 60$ . Bacteria concentrate in the splay regions and occasionally cross the bend region. (b) Experimental microscope images of bacterial trajectories [29] confirming our findings in (a). (c) A fully-developed stabilized undulation of the jet. Top: simulation result for  $N_p = 220$  at  $t = 500\tau$ . Graphical definitions of the undulation wavelength  $\lambda$ , undulation amplitude  $A$ , and jet width  $W_d$  are given. Bottom: Experimental results from Ref. [29]. The red sticks represent the pre-designed surface nematic field and blue sticks represent the bacteria. (d) Time evolution of  $A$  and  $\lambda$  of the jet in (c). (e) Time evolution of  $W_d$ ,  $C_l$  and  $\rho_j$  of the jet in (c). (f) The maximum value of swimmer density in the jet  $\rho_j^m$  and the average density in the stable jet  $\rho_j^s$  versus  $N_p$ . (g)  $A$  and  $\lambda$  of the wave in the fully developed region as functions of  $N_p$ . (h)  $\lambda$  as a function of  $\rho_j$ . The red solid line is the fit  $\lambda \propto 1/\sqrt{\rho_j^s - \rho_j^{sc}}$ . Inset: The collapse of the data  $\text{ave}(\lambda)/\sqrt{\rho_j^s - \rho_j^{sc}}$ .

the simulation box. Then the swirl of  $N_p = 90$  particles begins to undulate due to the bend instability associated with the extensile activity [22, 24, 26, 27]. Some swimmers evade the most prominent protrusions, while the others continue to swirl ( $t = 1160\tau$  in Fig. 1(f))—this again reproduces the experiment [26].

We next examine a different system where a periodic C-patterned surface is used to guide a unidirectional bacterial flow (namely a “bacterial jet”) in an LN, as reported in Ref. [29]. When a small population of microswimmers ( $N_p \leq 100$ ) are over a periodic splay-bend pattern, they will migrate into the splay regions and form a unidirectional jet along the converging direction (i.e., the  $+x$  direction, see Fig. 2(a)). Once the polar jet is established in the splay regions, the swimmers become trapped and rarely enter the bend region. These key features of the experiment [29] are well reproduced (Figs. 2(a) and 2(b)). As more bacteria accumulate in the splay band ( $N_p \geq 120$ ), the initially straight jet develops a periodic undulation, leading to the distortion of the nearby nematic field (Fig. 2(c) and Supplementary Video 2). This behavior is also clearly observed in the experiment [29]. To quantify this transition, we introduce microswimmer concentration (or population density) within the jet defined as  $\rho_j = N_p/(C_l W_d)$ , where  $C_l$  and  $W_d$  are the contour length and the width of the jet,

respectively (Fig. 2(c)). In Figs. 2(d) and 2(e), we plot the evolution of the amplitude  $A$ , the wavelength  $\lambda$ ,  $W_d$ , and  $\rho_j$  for  $N_p = 220$ . The swimmers gradually accumulate in the splay region and form a jet. At  $t = 200\tau$ ,  $A$  and  $C_l$  starts to grow, implying the onset of instability. In the wavy jet state,  $A$  and  $C_l$  of the undulation increase linearly before reaching a plateau, while its wavelength  $\lambda$  remains stable (Figs. 2(d) and 2(e)). As the undulation grows, the microswimmer density  $\rho_j$  dilates, leading to a lower effective active stress. Therefore, the undulation will stop growing when the active stress is balanced by the associated free energy cost. This wavy jet propagates at a constant phase velocity along the  $+x$  axis once its structure is stabilized (Supplementary Video 2). The forward advancing of the undulation wave agrees with the experiment [29, 53], with details further discussed in a separate work [53].

We record the maximum value of density in the jet as  $\rho_j^m$  (when  $W_d$  becomes minimum), and the average density of the steady wave  $\rho_j^s$  as a function of  $N_p$  in Fig. 2(f). There is a competition between the bend-induced active torque and the free energy cost of the undulation. The higher the microswimmer concentration  $\rho_j$  is, the higher the effective active stress would be. When  $\rho_j^m$  reaches the threshold  $\rho_j^0 \approx 0.50$ , the bend undulation becomes unstable and will grow. The critical concentration for

the onset of the undulation is approximately  $\rho_j^0 \approx 0.50$ , at which  $N_p \approx 120$ , corresponding to  $4.45 \times 10^{10} \text{m}^{-2}$  in SI units, which is close to the critical density reported in Ref. [29], where  $\rho_j^0 = 2.36 \times 10^{10} \text{m}^{-2}$ . Note that the threshold density for the spiral-pattern (Fig. 1) is  $\rho_j^0 \approx 0.1$ , which is lower than that in the C-pattern system. This trend is consistent with the experiment:  $\rho_j^0 \approx 0.57 \times 10^{10} \text{m}^{-2}$  in the spiral-pattern system compared to  $\rho_j^0 = 2.36 \times 10^{10} \text{m}^{-2}$  in the C-pattern system [26]. Both  $\rho_j^s$  and  $\rho_j^m$  decrease as  $N_p$  increases once  $\rho_j^m$  is above the threshold, as a result of fast growth of  $C_l$  and  $W_d$  [29].

We further measure the steady values of  $A$  and  $\lambda$  for stable propagating jets, straight or wavy, and present their dependence on the microswimmer population  $N_p$  and its concentration within the stable jet  $\rho_j^s$  in Figs. 2(g) and 2(h). When  $120 \leq N_p \leq 220$ , which corresponds to  $0.37 \leq \rho_j \leq 0.44$ , the wavelength scales as  $\lambda \propto 1/\sqrt{\rho_j - \rho_c}$ , with  $\rho_j^{sc} = 0.34$ . This relationship arises from the balance between active torque and elastic torque, consistent with Refs. [24, 29, 54]. When  $N_p > 220$ , the concentration  $\rho_j^s$  reaches a plateau around 0.36, at which  $W_d$  and  $A$  increase slowly, while  $\lambda$  is constantly around 29.05 (Figs. 2(f) and 2(h)). This suggests that the effective active stress is saturated when  $N_p > 220$ . A further increase in  $N_p$  (further decrease in  $\rho_j$ ) causes the swimmers to escape from the protrusions of the wave, leading to the rupture of the wave, as shown in [Supplementary Video 3](#) for  $\rho_j^s = 0.36$  ( $N_p = 280$ ). We record values only before wave rupture, where  $\lambda$  is determined by  $\rho_j^s$ .

Compared to the mean-field-like approach used in Ref. [29], our particle-based method is numerically stable and can handle sharp boundaries between bacteria-rich phase (region) and bacteria-depleted phase. The key advantage of our agent-based model lies in its ability to resolve individual swimmers. This allows us to faithfully capture the finite width of the undulation band and the rupture of the undulation, providing additional insights into the dynamics of the LN.

## B. Interactions with Topological Defects

Defects widely exist in active turbulence when activity dominates over LC elasticity. In a 2D LN, bacteria tend to accumulate at the cores of  $+1/2$  defects and are depleted from the cores of  $-1/2$  defects, as demonstrated through both experimental observations and continuum simulations [27]. In 3D active nematics, disclination lines can form closed loops [55]. These loops are influenced by a self-propulsion velocity based on their local profiles, causing the defect loops to expand, contract, or buckle over time [56–58]. 3D LNs are different from 3D active nematics, in which activity coefficient can be assumed uniform. Microswimmers in 3D LNs can aggregate at or deplete from certain defects, which can lead to modulated activity. Therefore, we expect richer defect dynamics in

3D LNs.

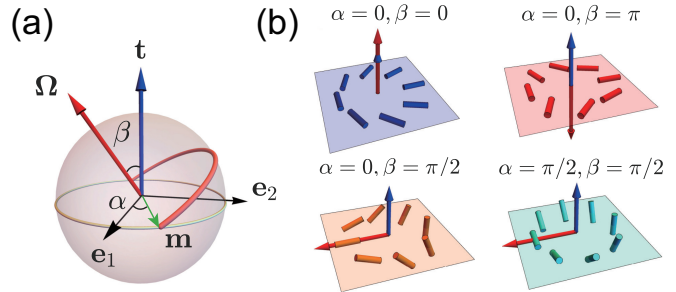


FIG. 3. Schematic representation of the local director profile for a winding of a line or loop defect. (a) Order parameter space with the pink path indicating the trajectory of the director ends starting from the origin. (b) Typical windings:  $+1/2$  wedge with  $\alpha = 0, \beta = 0$ ;  $-1/2$  wedge with  $\alpha = 0, \beta = \pi$ ; radial twist winding with  $\alpha = 0, \beta = \pi/2$ ; and tangential twist winding with  $\alpha = \pi/2, \beta = \pi/2$ .

Before we study the interactions between microswimmers and loop defects, we first characterize the structure of the defects, as illustrated in Fig. 3. The local director profile of a winding of a defect loop can be written as [56]:

$$\mathbf{n} = \cos \frac{1}{2} \phi \mathbf{m} + \sin \frac{1}{2} \phi (\cos \beta \mathbf{t} \times \mathbf{m} + \sin \beta \mathbf{t}), \quad (13)$$

where unit vector  $\mathbf{t}$  denotes the tangent vector of the defect at the winding, and  $\beta$  is the angle between  $\mathbf{t}$  and the normal  $\Omega$ , around which all directors on the cross section of the defect line rotate. The graphical definitions of these vectors are shown in Fig. 3(a). The vector  $\mathbf{m}$  is orthogonal to  $\Omega$  and  $\mathbf{t}$ . Additionally,  $\mathbf{e}_1$  and  $\mathbf{e}_2$  are a pair of orthogonal basis on the plane perpendicular to  $\mathbf{t}$ , and we denote  $\phi = 0$  by  $\mathbf{e}_1$ . Then the orientation  $\mathbf{m}$  can be expressed as  $\mathbf{m} = \cos \alpha \mathbf{e}_1 + \sin \alpha \mathbf{e}_2$ . A winding with  $\beta = \pi/2$  is a pure-twist winding, and those with  $\beta = 0$  and  $\pi$  are called wedges (Fig. 3(b)). The offset angle  $\alpha$  distinguish the “twist type” as “radial twist” if  $\alpha = 0$  or  $\pi$  and “tangential twist” if  $\alpha = \pi/2$  (Fig. 3(b)).

In the simulation we first study a wedge-twist loop with its winding angle  $\beta$  continuously increasing from 0 to  $\pi$  on one half of the loop and decreasing back to 0 on the other half. The active force will concentrate on and thereby mobilize the  $+1/2$  winding (where  $\beta = 0$ ) along its orientation (head direction). Therefore, the defect loop may exhibit expansion or shrinkage depending on the orientation of the  $+1/2$  wedge.

We first choose the orientation of the  $+1/2$  wedge to point outward (i.e., along the  $-x$  direction, see Fig. 4(a)). This kind of loop defect can be prepared in a nematic cell with homeotropic-anchoring walls, and the nematic director within the plane of the loop is in the  $x$ -direction (Fig. 4(a)). To highlight the critical role of the polar nature of the swimmers and their aggregation in 3D LNs, we tune two important parameters in the simulation: the intrinsic swimming velocity  $v_0$  and the characteristic size of the swimmers  $\sigma$  ( $l/\sigma = 2$ ). The range of swimmer

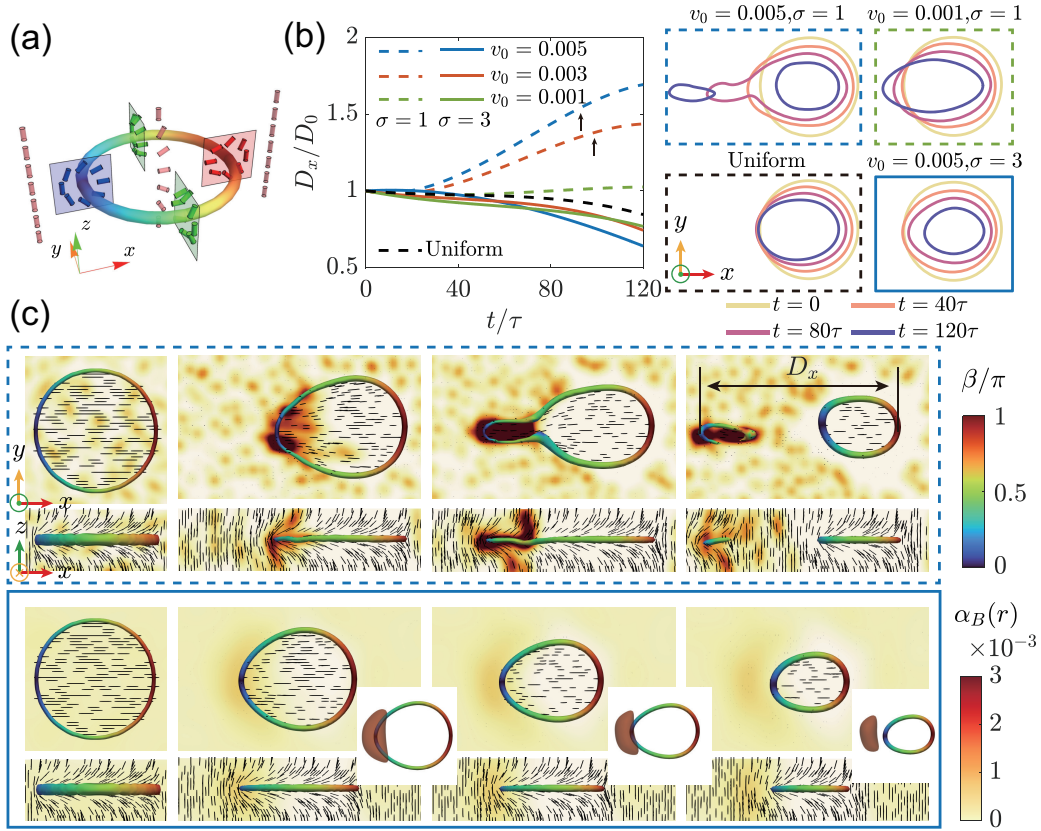


FIG. 4. Dynamics of a wedge-twist loop defect in a homeotropic-anchoring cell. (a) The schematic of the loop defect. The color of the loop indicates the angle  $\beta$  (colorbar is shown in panel (c)). (b) The evolution of the lateral size  $D_x$  (defined in (c)) of the defect for different combinations of  $v_0$  and  $\sigma$ . The black arrows indicate the breakup of the loops. The colored contours represent the superimposed loops at various time snapshots, illustrating their morphodynamics. For the uniform case, particle positions are fixed, with a constant pairwise distance  $\sigma = \sqrt[3]{L_x L_y L_z / N_p}$ . (c) The simulation snapshots showing the midplane colored by the active strength,  $\alpha_B(\mathbf{r})$ , to indicate the presence of the swimmers. The defect loop is colored according to the twisted angle  $\beta$ . The black lines represent the director field of the nematic background. The top panel, enclosed in the blue dashed box, corresponds to  $v_0 = 0.005$  and  $\sigma = 1$  (Supplementary Video 4), while the bottom panel, enclosed in the solid blue box, corresponds to  $v_0 = 0.005$  and  $\sigma = 3$ . The insets show the isosurface of  $\alpha_B(\mathbf{r}) = 6 \times 10^{-4}$ , highlighting the swimmer cluster.

speeds ( $0 \leq v_0 \leq 0.005$ ) is consistent with values observed in biological systems, such as bacterial swimming speeds reported to range from 0 – 16  $\mu\text{m/s}$  in experiments [24, 31, 36]. Although the size of individual swimmers is underestimated in our model (0.2 – 8  $\mu\text{m}$  from experiments [24, 31, 36]) due to the point-force assumption—similar to those in Refs.[27–29]—this approach effectively captures the key phenomena identified in the previous section. We record the lateral size of the defect loop evolution,  $D_x$ , and the shape evolution of the loop in Fig. 4(b).

From the colormap of  $\alpha_B(\mathbf{r})$  in Fig. 4(c), we observe that the microswimmers concentrate in splay regions, particularly near the  $+1/2$  wedge. As a result, the loop is deformed by the active flow, forming a sharp corner pointing toward the  $-x$  axis. The increased local curvature of the defect loop further amplifies the splay deformation, thereby attracting more microswimmers. In the case of a large swimming velocity and a small swimmer size ( $v_0 = 0.005$ ,  $\sigma = 1$ ), as shown in Fig. 4(b) and the upper panel of Fig. 4(c), the particles rapidly aggregate

within a small region near the  $+1/2$  wedge. The dense clustering of the swimmers generates a larger active flow compared to the uniform activity case, while the depletion of the particles near the  $-1/2$  wedge (where  $\beta = \pi$ ) has a minimal effect. Consequently, instead of shrinking as in the uniform activity case, the loop continuously expands. Eventually, the small segment of the loop is dragged so strongly that the loop engenders a child loop moving along the  $-x$  with a higher speed, leading to the steady increase of  $D_x$  (Fig. 4(c)). Interestingly, when both the swimming velocity and the repulsive distance are large ( $v_0 = 0.005$ ,  $\sigma = 3$ ), the behavior of the loop changes. In the early stage, the swimmers also rapidly aggregate near the leftmost side of the loop where  $\beta \approx 0$ . However, the larger separations between the swimmers reduce the equivalent activity  $\alpha_B$  and weaken the active flow, which cannot compete with the elastic force that tends to shrink the loop. As a result, the swimmer cluster is left ahead of the loop, and the loop annihilates faster than in the uniform activity case.

A different type of wedge-twist loop with the  $+1/2$



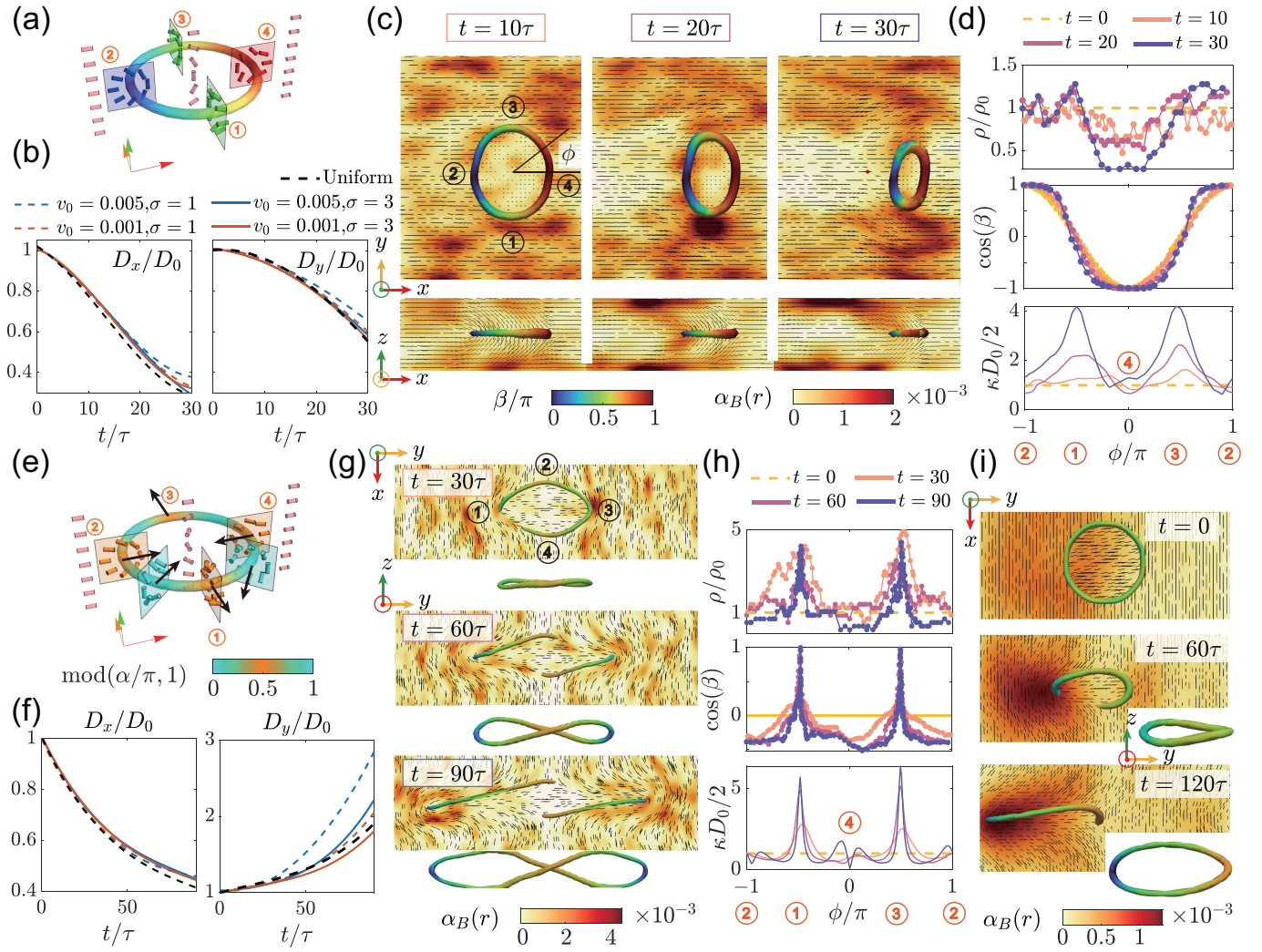


FIG. 5. Dynamics of a wedge-twist and a pure-twist loop defect in a planar-anchoring cell. (a) Schematic of the wedge-twist loop defect with its  $+1/2$  wedge pointing inward. (b) Evolution of the normalized  $D_x$  and  $D_y$  for different values of  $v_0$  and  $\sigma$ . (c) Snapshots at various time intervals to show the evolution of the defect loop and the distribution of the swimmers for  $v_0 = 0.005$  and  $\sigma = 1$ , colored by  $\alpha_B(\mathbf{r})$  in the midplane along the  $z$  and  $y$  directions. (d), (h) Normalized swimmer density  $\rho$ , twist angle  $\beta$ , and loop curvature  $\kappa$  plotted along the azimuthal direction of the loop at various time intervals. (e) Schematic of the pure-twist loop defect. The black arrows show the direction of the active flow if a uniform activity is assumed. (f) Evolution of the normalized  $D_x$  and  $D_y$  for different values of  $v_0$  and  $\sigma$ . (g) Projections of the defect loop in the  $xy$  and  $yz$  planes, along with the swimmer distribution in the midplane, for  $v_0 = 0.005$  and  $\sigma = 1$ . (i) A pure-twist loop surrounded by the same director configuration as in (e) but with an initially nonuniform distribution of the swimmers with total population  $N_p = 600$  ( $v_0 = 0.002$  and  $\sigma = 3$ ). The left side of the simulation box ( $y < N_y/2$ ) contains triple as many microswimmers as the right side ( $y \geq N_y/2$ ). The dynamics of the loop are demonstrated through changes in its position and structure, as characterized by the angle  $\beta$ .

wedge pointing inward (along the  $+x$  direction, see Fig. 5(a)) can be prepared in a nematic cell with planar-anchoring walls. The nematic director within the plane of this type of defect is in the  $z$ -direction (Fig. 5(a)). Therefore, the active force acting on the wedge promotes the shrinking of the defect, which will appear to be elongated in the  $y$ -direction [56]. In our simulation, the difference between this type of loop and the above-mentioned loop (Fig. 4(a)) is not only the direction of the active force [56], but also the evolution of the swimmer distribution, and the loop structure and its shape (Figs. 5(c) and 5(d) and

Supplementary Video 5). From the snapshots in Fig. 5(c) and the azimuthal distribution of the swimmer density  $\rho$  (Fig. 5(d)), the microswimmers concentrate at the two ends of the loop along the  $y$ -direction, where the windings are of pure-twist type with  $\beta \approx \pi/2$ . The shrinking of the loop results in the steady increase of the local curvature of these pure-twist windings (Fig. 5(d)). The swimmer density marginally exceeds the initial density  $\rho_0$  near the  $+1/2$  wedge but continuously decreases around the  $-1/2$  wedge. When viewed in the  $xz$  plane, the swimmers swim toward the two substrates, where splay deformation dom-

inates, and are thereafter trapped, which resembles the trapping of microswimmers in the C-pattern [29] (Fig. 2). The shrinking dynamics of the loop does not exhibit significant differences between different sets of  $v_0$  and  $\sigma$  (Fig. 5(b)). However, when the swimming velocity is high while its excluded-volume size is small ( $v_0 = 0.005$  and  $\sigma = 1$ ), loop-shrinking dynamics are slightly slowed down, as the swimmers can quickly migrate toward the boundaries and weaken the active flows.

We further study pure-twist loops in our simulation. For a pure-twist loop,  $\beta = \pi/2$  everywhere and  $\alpha$  continuously winds  $4\pi$  along the loop (Fig. 5(e)). For a uniform activity, the loop expands at position 1 and 3, where the windings are of radial twist type with the active flow pointing outward, and shrinks at position 2 and 4, where the windings are of radial twist type with active flow pointing inward. The out-of-plane flow at other windings of the loop causes the loop to buckle at its four diagonal directions [56]. From Figs. 5(f) to 5(h) and [Supplementary Video 6](#), the swimmers gradually concentrate at position 1 and 3 where  $\beta$  angle decreases over time, and their curvatures increase as the loop becomes stretched along the  $y$ -direction. Loop elongation  $D_y$  exhibits the fastest growth rate for high swimming velocity and small swimmer size ( $v_0 = 0.005$  and  $\sigma = 1$ ), whereas its shrinkage along the  $x$ -direction is less sensitive to these parameters. Motivated by the fact that swimmer density variation around the defect loop can impact its dynamics, we create a nonuniform initial distribution of the swimmers in the simulation box, with the  $+y$  half of the box populated with  $3N_p/4$  swimmers and the  $-y$  half of the box with  $N_p/4$  swimmers (Fig. 5(i)). In the high-density region, the bacteria migrate to position 1 over time, and the loop undergoes a torsional buckling, causing the immersed portion of the loop to be drawn along the  $-y$ -direction and twisted significantly. Meanwhile, swimmers in the  $+y$  half of the box initially aggregate around position 3 at  $t = 60\tau$ . However, this small cluster of swimmers are unable to stretch the loop along the  $+y$ -direction and are eventually dispersed ( $t = 120\tau$  in Fig. 5(i)). As a result, the defect loop undergoes a net displacement in the  $-y$  direction. The unbalanced torsional twist in the  $+y$  and  $-y$  halves of the loop causes it to eventually tumble into the  $yz$  plane, transforming the loop from an initially pure-twist configuration into a wedge-twist configuration. This new configuration exhibits a similar nematic structure to the wedge-twist loop in the homeotropic cell (Fig. 5(i), Fig. 4(a)).

Our results reveal that not only do the local profiles of the defect loops influence their dynamics in an LN, but also the distribution of the active units plays a crucial role. Their interplay can give rise to rich dynamics and lead to different destinies of the defects.

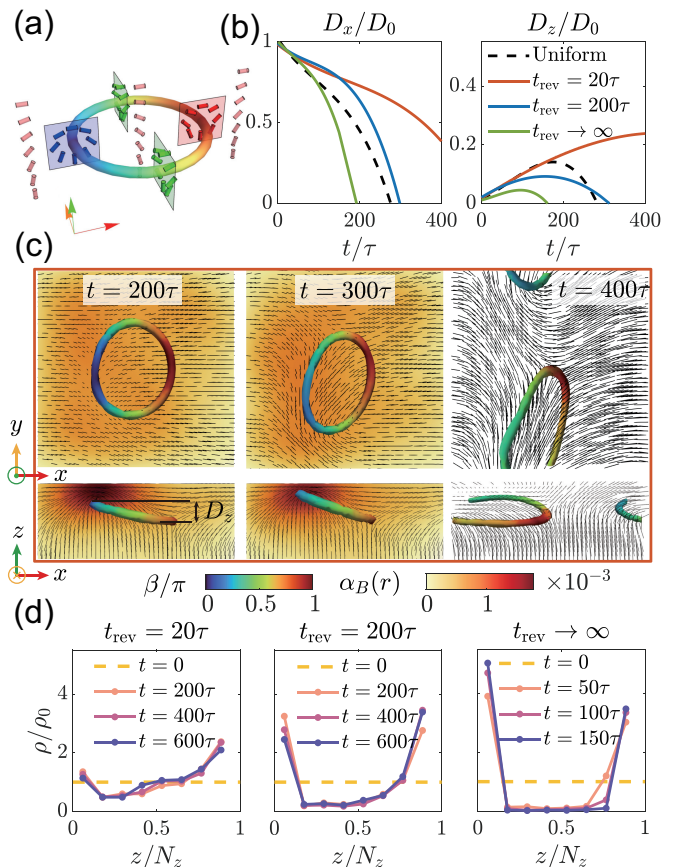


FIG. 6. Interactions of microswimmers with a wedge-twist loop in a hybrid cell with non-penetrable bounding surfaces.  $v_0 = 0.003$ ,  $\sigma = 3$ . (a) The schematic of a wedge-twist loop in a hybrid cell with its  $+1/2$  wedge pointing upward. (b) The evolution of the lateral size,  $D_x$  and  $D_z$ , is analyzed for a range of  $t_{\text{rev}}$  spanning from 0 (uniform) to  $\infty$ . (c) Snapshots at various time intervals to show the evolution of the loop defect and the distribution of the swimmers for  $t_{\text{rev}} = 20\tau$ . (d) The density distribution along the  $z$  direction is shown for  $t_{\text{rev}} = 20\tau$ ,  $t_{\text{rev}} = 200\tau$ , and  $t_{\text{rev}} \rightarrow \infty$ . For the uniform case, note that  $\rho/\rho_0$  remains consistently equal to 1.

### C. Density Pumping in a Hybrid Nematic Cell

In the above discussions, the swimmers can re-enter the simulation box via periodic boundary conditions. This simplification has helped us to focus on the dynamics of the defects immersed in an environment with a constant overall microswimmer density, analogous to an “ $\mu VT$  ensemble”. We now focus on a more realistic situation that the microswimmers are allowed to aggregate on boundary walls. It is observed that bacteria can switch their swimming direction by  $180^\circ$  in an anisotropic environment, with their flagella switching sides by backtracking or forming two opposing tails to perform a “tug-of-oars” mechanism [16, 31, 36, 59, 60]. This behavior arises due to the suppression of the run-and-tumble motion typically observed in isotropic solutions [61–63]. For an LC environment, the reversal time  $t_{\text{rev}}$  varies depending on the type and size of the bacterium, the con-

centration of the LC solution, and the anchoring type and strength of the boundary surfaces. For instance,  $t_{\text{rev}} \sim 30 - 300$  s for *B. subtilis* in lyotropic disodium cromoglycate (DSCG) over a wide range of concentrations (12.5 wt %–18.5 wt %) [27, 60]; and  $t_{\text{rev}} \sim 1 \times 10^4$  s for *B. subtilis* in DSCG solutions with patterned anchoring on the top and bottom surfaces [36];  $t_{\text{rev}} \sim 7$  s for *P. mirabilis* in the bulk of 15 wt % DSCG solution with homeotropic or hybrid surface anchoring [31]; Moreover, *B. subtilis* can swim horizontally near the homeotropically anchored surfaces and switch their swimming direction either by backtracking or through an horizontal-vertical-horizontal mechanism with  $t_{\text{rev}} \sim 2 - 12$  s in a nematic DSCG solution [36].

In our simulation, the swimming direction switches as  $\mathbf{p}_i \rightarrow -\mathbf{p}_i$  at  $t = t_{n,i}$ , where the time interval between two consecutive switches,  $\Delta T_{n,i} \equiv t_{n,i} - t_{n-1,i}$ , is given by  $\Delta T_{n,i} = -\ln(U)/m$ . Here,  $U$  is a random number in the range  $[0, 1)$ , and the switching of direction is modeled as independent events occurring with an average rate  $m = 1/t_{\text{rev}}$ . When  $t_{\text{rev}} \rightarrow 0$ , the system reduces to a uniform active nematic [27]. Conversely, for  $t_{\text{rev}} \rightarrow \infty$ , swimmers gradually adhere to the bounding surfaces after starting from a uniformly distributed initial state.

Here we consider a hybrid wall with the top and bottom surface imposing planar and homeotropic anchoring condition, respectively. The  $+1/2$  wedge on a wedge-twist loop in this type of cell points towards the  $+z$  direction (Fig. 6(a)). The loop size shows non-monotonic behavior as  $t_{\text{rev}}$  changes. If  $t_{\text{rev}} \rightarrow 0$  (uniform activity), the vertical active flow around the  $+1/2$  wedge pins the loop segment and lifts this piece along the  $+z$  direction, causing the loop to tilt out of the  $xy$  plane. This leads to a decrease in  $D_x$  and an initial increase in  $D_z$ . However, as the lifting of the  $+1/2$  wedge is stopped by the top confinement surface, elastic relaxation begins to dominate, resulting in a decrease in  $D_z$  (Fig. 6(b)). As  $t_{\text{rev}}$  increases to  $20\tau$  ( $\approx 2.5$  s), the shrinking process slows down. During this phase, many bacteria are pumped into the upper region of the cell (Figs. 6(c) and 6(d), see [Supplementary Video 7](#)), congregating around the  $+1/2$  wedge. This triggers a bend instability, which prevents the annihilation of the defect loop. Consequently,  $D_x$  does not approach zero, and  $D_z$  continues to increase over time. At even higher  $t_{\text{rev}}$  values (e.g.,  $t_{\text{rev}} = 200\tau \approx 25$  s), more swimmers accumulate near the bounding surfaces ( $z/N_z = 0, 1$  in Fig. 6(d)), waiting for their next reversal to re-enter the bulk. This reduces the population density of the swimmers in the bulk, and the shrinking of the loop is therefore the fastest. Finally, if  $t_{\text{rev}} \rightarrow \infty$ , the swimmers initially accumulate in the upper region of the cell around the  $+1/2$  wedge. However, most of them eventually make a U-turn at the head of the  $+1/2$  defect and migrate toward the bottom surface, leading to their accumulation at the bottom surface, which exhibits a higher concentration than that near the top surface. This implies that microswimmers could accumulate in homeotropic-anchoring walls where bend deformation dominates. As

a consequence of the depletion of bacteria in the bulk at the early stage ( $t < 150\tau$  in Fig. 6(d)), the loop shrinks the fastest and is lifted by the shortest distance. Further experimental validation is needed to investigate bacterial reversal near different types of anchoring surfaces and to test how this influences disclination lines or loops in the bulk.

## D. Discussion

We have developed a hybrid method to combine a particle-based approach for the microswimmers and a well-validated hydrodynamic model for the continuous LC phase. Our method can work with both 2D and 3D systems. A similar hybrid approach has been shown successful in simulating the dynamics of active chemotactic droplets dispersed in a chemical field [64]. This method conveniently models uniaxial swimmers (which is characterized by the shape parameter  $\epsilon$ ) as force dipoles. More sophisticated models, such as spherical squirmers, have been used in literature [33, 34]. Our method will become more advantageous when the microswimmers are small and their anchoring is not essential or when the population of the microswimmers is enormous. Compared to other field models that treat the bacteria as either another continuous phase [29] or a concentration field [27–29], our method treats the microswimmers as discrete particles without doing mean-field averages, therefore retaining the particle-level resolution and exhibiting robustness and numerical stability over a wide range of microswimmer populations. This allows us to examine how microswimmers transition from individual dynamics to collective dynamics as their population density increases. Because our method accurately accounts for the hydrodynamics of the background LC, we are able to reproduce the stabilized undulations of jets and swirls reported in the experiments. Furthermore, the extension to 3D systems enables comparisons to more realistic experimental studies, including the effects of surface anchoring strength, hydrodynamic boundary condition, and 3D nematic field and confinement. There are many potential applications of our work in extended areas, including the study of how anisotropic elastic constants affect the dynamics of the microswimmers, microswimmers interacting with loop defects with nonzero topological charge [65, 66] or solitonic structures in cholesteric LCs [66, 67], interactions between microswimmers in active turbulent state [55, 58], impact of external fields [68].

## ACKNOWLEDGMENTS

R.Z. acknowledges support from Hong Kong Research Grants Council via grant no. 16306924. Z.Y. acknowledges support from National Natural Science Foundation of China No. 12374219.



**Supplementary Video 1:** Steady circulation and subsequent undulation of bacteria in a spiral-patterned thin film, as shown in [Fig. 1](#).

**Supplementary Videos 2 & 3:** Stabilized undulation observed in the splay region for  $N_p = 220$  and  $N_p = 280$ , respectively, as illustrated in [Fig. 2](#).

**Supplementary Video 4:** Dynamics of bacteria and loops within a cylindrical splay cell, corresponding to [Fig. 4](#).

**Supplementary Videos 5 & 6:** Dynamics of bacteria and loops within cylindrical bend and cylindrical twist cells, respectively, as depicted in [Fig. 5](#).

**Supplementary Video 7:** Dynamics of bacteria and loops in a cylindrical reversed hybrid cell as shown in [Fig. 6](#).

- [1] M. C. Marchetti, J.-F. Joanny, S. Ramaswamy, T. B. Liverpool, J. Prost, M. Rao, and R. A. Simha, *Hydrodynamics of soft active matter*, *Rev. modern physics* **85**, 1143 (2013).
- [2] D. Saintillan, *Rheology of active fluids*, *Annu. review fluid mechanics* **50**, 563 (2018).
- [3] G. Gompper, R. G. Winkler, T. Speck, A. Solon, C. Nardin, F. Peruani, H. Löwen, R. Golestanian, U. B. Kaupp, L. Alvarez, *et al.*, *The 2020 motile active matter roadmap*, *J. Physics: Condens. Matter* **32**, 193001 (2020).
- [4] C. Bechinger, R. Di Leonardo, H. Löwen, C. Reichhardt, G. Volpe, and G. Volpe, *Active particles in complex and crowded environments*, *Rev. modern physics* **88**, 045006 (2016).
- [5] C. W. Chan, D. Wu, K. Qiao, K. L. Fong, Z. Yang, Y. Han, and R. Zhang, *Chiral active particles are sensitive reporters to environmental geometry*, *Nat. Commun.* **15**, 1406 (2024).
- [6] S. S. Suarez and A. Pacey, *Sperm transport in the female reproductive tract*, *Hum. reproduction update* **12**, 23 (2006).
- [7] V. Kantsler, J. Dunkel, M. Blayney, and R. E. Goldstein, *Correction: Rheotaxis facilitates upstream navigation of mammalian sperm cells*, *Elife* **3**, e03521 (2014).
- [8] I. I. Smalyukh, J. Butler, J. D. ShROUT, M. R. Parsek, and G. C. L. Wong, *Elasticity-mediated nematiclike bacterial organization in model extracellular DNA matrix*, *Phys. Rev. E* **78**, 030701 (2008).
- [9] H.-C. Flemming and J. Wingender, *The biofilm matrix*, *Nat. reviews microbiology* **8**, 623 (2010).
- [10] D. J. Lemon, X. Yang, P. Srivastava, Y.-Y. Luk, and A. G. Garza, *Polymertropism of rod-shaped bacteria: movement along aligned polysaccharide fibers*, *Sci. reports* **7**, 7643 (2017).
- [11] A. Repula, E. Abraham, V. Cherpak, and I. I. Smalyukh, *Biotropic liquid crystal phase transformations in cellulose-producing bacterial communities*, *Proc. National Acad. Sci.* **119**, e2200930119 (2022).
- [12] W. Gao and J. Wang, *Synthetic micro/nanomotors in drug delivery*, *Nanoscale* **6**, 10486 (2014).
- [13] K. J. Rao, F. Li, L. Meng, H. Zheng, F. Cai, and W. Wang, *A force to be reckoned with: a review of synthetic microswimmers powered by ultrasound*, *Small* **11**, 2836 (2015).
- [14] Z. Wu, Y. Chen, D. Mukasa, O. S. Pak, and W. Gao, *Medical micro/nanorobots in complex media*, *Chem. Soc. Rev.* **49**, 8088 (2020).
- [15] W. Masocha, B. Robertson, M. E. Rottenberg, J. Mhlanga, L. Sorokin, K. Kristensson, *et al.*, *Cerebral vessel laminins and IFN- $\gamma$  define Trypanosoma brucei brucei penetration of the blood-brain barrier*, *The J. clinical investigation* **114**, 689 (2004).
- [16] A. Patteson, A. Gopinath, M. Goulian, and P. Arratia, *Running and tumbling with E. coli in polymeric solutions*, *Sci. reports* **5**, 15761 (2015).
- [17] J. R. Gomez-Solano, A. Blokhuis, and C. Bechinger, *Dynamics of Self-Propelled Janus Particles in Viscoelastic Fluids*, *Phys. Rev. Lett.* **116**, 138301 (2016).
- [18] C.-k. Tung, C. Lin, B. Harvey, A. G. Fiore, F. Ardon, M. Wu, and S. S. Suarez, *Fluid viscoelasticity promotes collective swimming of sperm*, *Sci. reports* **7**, 3152 (2017).
- [19] D. Yuan, Q. Zhao, S. Yan, S.-Y. Tang, G. Alici, J. Zhang, and W. Li, *Recent progress of particle migration in viscoelastic fluids*, *Lab on a Chip* **18**, 551 (2018).
- [20] K. Ishimoto and E. A. Gaffney, *Hydrodynamic clustering of human sperm in viscoelastic fluids*, *Sci. Reports* **8**, 15600 (2018).
- [21] S. Liu, S. Shankar, M. C. Marchetti, and Y. Wu, *Viscoelastic control of spatiotemporal order in bacterial active matter*, *Nature* **590**, 80 (2021).
- [22] C. Peng, T. Turiv, Y. Guo, Q.-H. Wei, and O. D. Lavrentovich, *Command of active matter by topological defects and patterns*, *Science* **354**, 882 (2016).
- [23] A. Kumar, T. Galstian, S. K. Pattanayek, and S. Rainville, *The motility of bacteria in an anisotropic liquid environment*, *Mol. Cryst. Liquid Cryst.* **574**, 33 (2013).
- [24] S. Zhou, A. Sokolov, O. D. Lavrentovich, and I. S. Aranson, *Living liquid crystals*, *Proc. National Acad. Sci.* **111**, 1265 (2014).
- [25] A. Sokolov, S. Zhou, O. D. Lavrentovich, and I. S. Aranson, *Individual behavior and pairwise interactions between microswimmers in anisotropic liquid*, *Phys. Rev. E* **91**, 013009 (2015).
- [26] R. Koizumi, T. Turiv, M. M. Genkin, R. J. Lastowski, H. Yu, I. Chaganava, Q.-H. Wei, I. S. Aranson, and O. D. Lavrentovich, *Control of microswimmers by spiral nematic vortices: Transition from individual to collective motion and contraction, expansion, and stable circulation of bacterial whirls*, *Phys. Rev. Res.* **2**, 033060 (2020).
- [27] M. M. Genkin, A. Sokolov, O. D. Lavrentovich, and I. S. Aranson, *Topological Defects in a Living Nematic Ensnare Swimming Bacteria*, *Phys. Rev. X* **7**, 011029 (2017).
- [28] M. M. Genkin, A. Sokolov, and I. S. Aranson, *Spontaneous topological charging of tactoids in a living nematic*, *New J. Phys.* **20**, 43027 (2018).
- [29] T. Turiv, R. Koizumi, K. Thijssen, M. M. Genkin, H. Yu, C. Peng, Q.-H. Wei, J. M. Yeomans, I. S. Aranson, A. Doostmohammadi, and O. D. Lavrentovich, *Polar jets of swimming bacteria condensed by a patterned liquid crystal*, *Nat. Phys.* **16**, 481 (2020).
- [30] P. C. Mushenheim, R. R. Trivedi, H. H. Tuson, D. B. Weibel, and N. L. Abbott, *Dynamic self-assembly of motile bacteria in liquid crystals*, *Soft Matter* **10**, 88 (2013).
- [31] P. C. Mushenheim, R. R. Trivedi, S. S. Roy, M. S. Arnold, D. B. Weibel, and N. L. Abbott, *Effects of confinement, surface-induced orientations and strain on dynamical behaviors of bacteria in thin liquid crystalline films*, *Soft Matter* **11**, 6821 (2015).
- [32] R. R. Trivedi, R. Maeda, N. L. Abbott, S. E. Spagnolie, and D. B. Weibel, *Bacterial transport of colloids in liquid crystalline environments*, *Soft Matter* **11**, 8404 (2015).
- [33] J. Lintuvuori, A. Würger, and K. Stratford, *Hydrodynamics Defines the Stable Swimming Direction of Spherical Swimmers in a Nematic Liquid Crystal*, *Phys. Rev. Lett.* **119**, 68001 (2017), publisher: American Physical Society.
- [34] B. Gautam and J. S. Lintuvuori, *Microswimmers Knead Nematics into Cholesterics*, *Phys. Rev. Lett.* **132**, 238301 (2024).

- [35] H. Chi, M. Potomkin, L. Zhang, L. Berlyand, and I. S. Aranson, *Surface anchoring controls orientation of a microswimmer in nematic liquid crystal*, *Commun. Phys.* **3**, 162 (2020).
- [36] S. Zhou, O. Tovkach, D. Golovaty, A. Sokolov, I. S. Aranson, and O. D. Lavrentovich, *Dynamic states of swimming bacteria in a nematic liquid crystal cell with homeotropic alignment*, *New J. Phys.* **19**, 055006 (2017).
- [37] S. D. Ryan, L. Berlyand, B. M. Haines, and D. A. Karpeev, *A Kinetic Model for Semidilute Bacterial Suspensions*, *Multiscale Model. Simul.* **11**, 1176 (2013).
- [38] C. Denniston, E. Orlandini, and J. Yeomans, *Lattice Boltzmann simulations of liquid crystal hydrodynamics*, *Phys. Review E* **63**, 056702 (2001).
- [39] H. Li, X.-q. Shi, M. Huang, X. Chen, M. Xiao, C. Liu, H. Chaté, and H. Zhang, *Data-driven quantitative modeling of bacterial active nematics*, *Proc. National Acad. Sci.* **116**, 777 (2019).
- [40] H. Li, H. Chaté, M. Sano, X.-q. Shi, and H. P. Zhang, *Robust Edge Flows in Swarming Bacterial Colonies*, *Phys. Rev. X* **14**, 041006 (2024).
- [41] J. S. Dai, *Euler–Rodrigues formula variations, quaternion conjugation and intrinsic connections*, *Mech. Mach. Theory* **92**, 144 (2015).
- [42] K. Ishimoto, *Jeffery’s orbits and microswimmers in flows: A theoretical review*, *J. Phys. Soc. Japan* **92**, 062001 (2023).
- [43] R. Zhang, T. Roberts, I. S. Aranson, and J. J. De Pablo, *Lattice Boltzmann simulation of asymmetric flow in nematic liquid crystals with finite anchoring*, *The J. Chem. Phys.* **144** (2016).
- [44] A. N. Beris and B. J. Edwards, *Thermodynamics of flowing systems: with internal microstructure*, 36 (Oxford University Press, USA, 1994).
- [45] K. Thijssen, L. Metselaar, J. M. Yeomans, and A. Doostmohammadi, *Active nematics with anisotropic friction: the decisive role of the flow aligning parameter*, *Soft Matter* **16**, 2065 (2020).
- [46] N. Darnton, L. Turner, K. Breuer, and H. C. Berg, *Moving fluid with bacterial carpets*, *Biophys. journal* **86**, 1863 (2004).
- [47] S. Edwards and J. Yeomans, *Spontaneous flow states in active nematics: a unified picture*, *Europhys. letters* **85**, 18008 (2009).
- [48] K. Drescher, R. E. Goldstein, N. Michel, M. Polin, and I. Tuval, *Direct measurement of the flow field around swimming microorganisms*, *Phys. Review Lett.* **105**, 168101 (2010).
- [49] M. Hintsche, V. Waljor, R. Großmann, M. J. Kühn, K. M. Thormann, F. Peruani, and C. Beta, *A polar bundle of flagella can drive bacterial swimming by pushing, pulling, or coiling around the cell body*, *Sci. reports* **7**, 16771 (2017).
- [50] A. V. Singh, Z. Hosseini-doust, B.-W. Park, O. Yasa, and M. Sitti, *Microemulsion-based soft bacteria-driven microswimmers for active cargo delivery*, *ACS nano* **11**, 9759 (2017).
- [51] B.-W. Park, J. Zhuang, O. Yasa, and M. Sitti, *Multifunctional bacteria-driven microswimmers for targeted active drug delivery*, *ACS nano* **11**, 8910 (2017).
- [52] Y. Alapan, O. Yasa, O. Schauer, J. Giltinan, A. F. Tabak, V. Sourjik, and M. Sitti, *Soft erythrocyte-based bacterial microswimmers for cargo delivery*, *Sci. robotics* **3**, eaar4423 (2018).
- [53] J. Wu, Z. Mou, M. Liu, Y. Li, R. Wang, Z. Asilehan, Q. Shi, Z. You, J. Jiang, R. Zhang, and C. Peng, *Programmable active traveling waves in living liquid crystals* (2025), in preparation.
- [54] S. Ramaswamy, *The mechanics and statistics of active matter*, *Annu. Rev. Condens. Matter Phys.* **1**, 323 (2010).
- [55] G. Duclos, R. Adkins, D. Banerjee, M. S. Peterson, M. Varghese, I. Kolvin, A. Baskaran, R. A. Pelcovits, T. R. Powers, A. Baskaran, et al., *Topological structure and dynamics of three-dimensional active nematics*, *Science* **367**, 1120 (2020).
- [56] J. Binysh, i. c. v. Kos, S. Čopar, M. Ravnik, and G. P. Alexander, *Three-Dimensional Active Defect Loops*, *Phys. Rev. Lett.* **124**, 088001 (2020).
- [57] C. Long, X. Tang, R. L. Selinger, and J. V. Selinger, *Geometry and mechanics of disclination lines in 3D nematic liquid crystals*, *Soft Matter* **17**, 2265 (2021).
- [58] N. Kralj, M. Ravnik, and i. c. v. Kos, *Defect Line Coarsening and Refinement in Active Nematics*, *Phys. Rev. Lett.* **130**, 128101 (2023).
- [59] M. Goral, E. Clement, T. Darnige, T. Lopez-Leon, and A. Lindner, *Frustrated ‘run and tumble’ of swimming Escherichia coli bacteria in nematic liquid crystals*, *Interface Focus* **12**, 20220039 (2022).
- [60] A. G. Prabhune, A. S. García-Gordillo, I. S. Aranson, T. R. Powers, and N. Figueroa-Morales, *Bacteria Navigate Anisotropic Media using a Flagellar Tug-of-Oars*, *PRX Life* **2**, 033004 (2024).
- [61] H. C. Berg and D. A. Brown, *Chemotaxis in Escherichia coli analysed by three-dimensional tracking*, *nature* **239**, 500 (1972).
- [62] K. Taute, S. Gude, S. Tans, and T. Shimizu, *High-throughput 3D tracking of bacteria on a standard phase contrast microscope*, *Nat. communications* **6**, 1 (2015).
- [63] N. Figueroa-Morales, R. Soto, G. Junot, T. Darnige, C. Douarce, V. A. Martinez, A. Lindner, and E. Clément, *3D Spatial Exploration by E. coli Echoes Motor Temporal Variability*, *Phys. Rev. X* **10**, 021004 (2020).
- [64] C. W. Chan, Z. Yang, Z. Gan, and R. Zhang, *Interplay of chemotactic force, Péclet number, and dimensionality dictates the dynamics of auto-chemotactic chiral active droplets*, *The J. Chem. Phys.* **161**, <https://doi.org/10.1063/5.0207355> (2024).
- [65] S. Čopar, J. Aplinc, i. c. v. Kos, S. Žumer, and M. Ravnik, *Topology of Three-Dimensional Active Nematic Turbulence Confined to Droplets*, *Phys. Rev. X* **9**, 031051 (2019).
- [66] L. N. Carenza, G. Gonnella, D. Marenduzzo, and G. Negro, *Rotation and propulsion in 3D active chiral droplets*, *Proc. National Acad. Sci.* **116**, 22065 (2019).
- [67] C. A. Whitfield, T. C. Adhyapak, A. Tiribocchi, G. P. Alexander, D. Marenduzzo, and S. Ramaswamy, *Hydrodynamic instabilities in active cholesteric liquid crystals*, *The Eur. Phys. J. E* **40**, 1 (2017).
- [68] M.-A. Boule, S. Rainville, and T. Galstian, *Dynamic guiding of bacteria in lyotropic chromonic liquid crystal using magnetic field*, *Mol. Cryst. Liquid Cryst.* **712**, 10 (2020).